

See discussions, stats, and author profiles for this publication at: <https://www.researchgate.net/publication/223994899>

Three-Dimensional Super-Localization and Tracking of Single Gold Nanoparticles in Cells

ARTICLE in ANALYTICAL CHEMISTRY · APRIL 2012

Impact Factor: 5.64 · DOI: 10.1021/ac300249d · Source: PubMed

CITATIONS

22

READS

66

5 AUTHORS, INCLUDING:



Yan Gu

Harvard University

12 PUBLICATIONS 162 CITATIONS

SEE PROFILE



Wei Sun

Washington University

41 PUBLICATIONS 639 CITATIONS

SEE PROFILE



Gufeng Wang

North Carolina State University

53 PUBLICATIONS 1,192 CITATIONS

SEE PROFILE



Ning jian Fang

lvyou university

68 PUBLICATIONS 956 CITATIONS

SEE PROFILE

Three-Dimensional Super-Localization and Tracking of Single Gold Nanoparticles in Cells

Yan Gu,[†] Xiaowei Di,[‡] Wei Sun,[†] Gufeng Wang,^{*,§} and Ning Fang^{*,†}

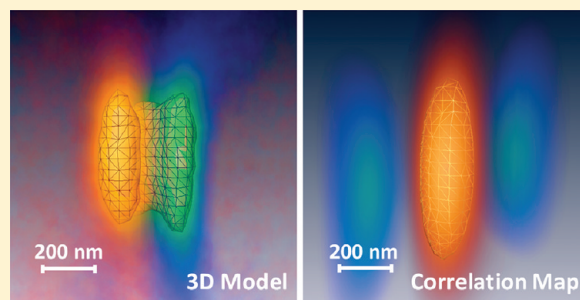
[†]Ames Laboratory, U.S. Department of Energy, and Department of Chemistry, Iowa State University, Ames, Iowa 50011, United States

[§]Department of Chemistry, North Carolina State University, Raleigh, North Carolina 27695, United States

[‡]College of Chemistry and Chemical Engineering, Inner Mongolia University, Hohhot 010021, China

S Supporting Information

ABSTRACT: We introduce a precise three-dimensional (3D) localization method of spherical gold nanoparticle probes using model-based correlation coefficient mapping. To accomplish this, a stack of sample images at different z-positions are acquired, and a 3D intensity profile of the probe serving as the model is used to map out the positions of nanoparticles in the sample. By using this model-based correlation imaging method, precise localization can be achieved in imaging techniques with complicated point spread functions (PSF) such as differential interference contrast (DIC) microscopy. We demonstrated the localization precision of 4–7 nm laterally and 16 nm axially for 40-nm gold nanospheres at an imaging rate of 10 frames per second. The 3D superlocalization method was applied to tracking gold nanospheres during live endocytosis events.



Many biological activities involve motions at the nanoscale, e.g., DNA polymerization,¹ motor protein stepping,^{2,3} and self-rotation of ATP synthase.⁴ Precisely locating and tracking optical probes are of vital importance in understanding these biological processes. Single fluorescent molecules and nanoparticles have been widely applied in these studies. For example, 8-nm steps of motor proteins have been resolved in live cells by tracking individual fluorescent particles.^{2,5} Ultrafine membrane compartments with a size ranging from 30 to 230 nm, which limits membrane protein diffusion, were revealed by single fluorescent molecule tracking.⁶ The localization precision of single molecules in such complex samples was typically 10–20 nm laterally and ~50 nm in the axial direction.^{7–11} It is worthwhile to point out that the localization precision directly determines the spatial resolution of optical imaging based on observing individual molecule/particle events that are temporally separated. For example, in stochastic optical reconstruction (STORM) or photoactivated localization (PALM) microscopy, dyes are switched “on” and “off” alternatively, allowing the localization of individual fluorophores with nanometer accuracy.^{9,12–14}

The major disadvantages of fluorescence-based imaging include photostability of fluorescent labels, e.g., photobleaching^{15,16} and blinking,^{16,17} and the interference to the natural cellular processes.^{8,18} An alternative approach is to use plasmonic gold nanoparticle probes, which display large optical cross sections near their surface plasmon resonance (SPR) frequencies, excellent photo- and chemical-stability, and good biocompatibility.^{19–22} In addition, they can be engineered into

different sizes and shapes, and their controllable surface chemistry allows them to be modified with a variety of chemically and biologically active molecules.

Gold nanoparticles have been imaged and tracked in live cells with a variety of techniques including bright-field microscopy,^{23,24} dark-field microscopy,^{25,26} photothermal interference contrast technique,^{27–29} differential interference contrast (DIC) microscopy,^{30,31} confocal Raman microscopy,³² and dynamic surface-enhanced Raman spectroscopy.³³ Among these techniques, DIC microscopy exhibits excellent detectability of small gold nanoparticles, thus the potential of serving as a powerful tool in single particle tracking studies. We recently used DIC microscope to track the endocytosis process of gold nanoparticles³¹ and visualized the rotational motion of gold nanorods in live cells and on cell membranes.^{34,35}

DIC microscope works on the principle of two-beam interferometry to gain information about the optical density of the sample. The interference nature makes it sensitive to see small features that display different refractive indices from its environment while insensitive to scattered light from surrounding cellular components. The result is that it enables the user to image both the nanoprobe and live cells with superior quality. A variety of cellular organelles that are invisible in other conventional microscopy such as bright-field microscopy becomes observable under a DIC microscope.³⁶

Received: January 24, 2012

Accepted: March 29, 2012

Published: March 29, 2012

The excellent detectability of nanoparticles and wide-field configuration gives excellent temporal resolution that are unparalleled by detection techniques based on raster scanning. Compared to scattering-based dark-field microscopy,^{25,26,37,38} imaging nanoparticles under the DIC microscope is less affected by other strong light scatterers, such as large vesicles and the edge of the nucleus, in the sample media.³⁹

More importantly, DIC microscopy allows for the use of the full numerical aperture (NA) of the microscope objective and condenser, resulting in the highest possible lateral and axial resolutions.^{40,41} The optical resolutions, defined as the full width at half-maximum (FWHM) of the intensity distribution of a point spread function (PSF), are⁴²

$$FWHM_{\text{Lateral}} = 0.51 \times \frac{\lambda}{NA} \quad (1)$$

laterally, and

$$FWHM_{\text{Axial}} = \frac{0.88 \times \lambda}{n - \sqrt{n^2 - NA^2}} \quad (2)$$

axially, where λ is the illumination wavelength, n is the refractive index of the immersion oil, and NA is the numerical aperture of the objective. In dark-field microscopy, the illumination is provided by a center-blocked, high-NA condenser (usually NA 1.2–1.4). The objective NA must be restricted (smaller than the condenser NA) to reject transmitted illumination beam, resulting in lower spatial resolution. Taking an oil-immersion ($n = 1.519$) objective with the NA restricted to 1.0 as an example, and assuming the illumination wavelength to be 545 nm, the lateral resolution in dark field microscopy is 278 nm, as compared to 199 nm in DIC microscopy (NA 1.4 for both condenser and objective). The axial resolution in dark field microscopy is 1277 nm, nearly 2.5 times the DIC axial resolution of 516 nm. Therefore, the image spot of a nanoparticle appears expanded both laterally and axially in dark-field microscopy when compared to the image spot in DIC microscopy (Supplementary Figure 1). In this sense, using DIC microscopy will yield much better precision in locating the centroids of the diffraction limited image spots of nanoparticle probes, especially in the axial direction.

Due to DIC microscopy's reliance on the principle of interference, nanoparticles show a half-bright and half-dark image superimposed on a gray background, which complicates the particle localization because simple Gaussian fitting of the image profile does not apply to the more complicated DIC PSF. To solve this problem, Gelles et al. developed a localization method by evaluating the cross correlation of the sample image with the kernel portion of a model particle image.⁴³ They demonstrated 1–2 nm precision laterally in tracking 190-nm plastic beads driven by kinesin motors under a DIC microscope. To the best of our knowledge, precisely tracking gold nanoparticles in 3D space to a few nanometer precision has not been demonstrated although there is an increasing demand to achieve this in the 3D matrix of biological samples.

In the present study, we systematically investigated the 3D PSF of gold nanoparticles in DIC microscopy and introduced an algorithm to locate gold nanoparticles in 3D space. The localization precision of 4–7 nm laterally and 16 nm axially for 40-nm gold nanospheres was achieved with an imaging rate of 10 frames per second and a vertical step size of 40 nm. The temporal resolution of 3D localization was in the range of

seconds, which was the time needed to record a stack of z-slices through the sample volume. We also demonstrated the application of this method in the tracking gold nanoparticles in live cells during the endocytosis events.

■ EXPERIMENTAL SECTION

Sample Slides. 40-nm gold nanoparticle colloid solutions were purchased from BBI International (Cardiff, UK). Positively charged amino silane-coated glass coverslips were prepared by modifying 22 mm × 22 mm No. 1.5 coverslips (Corning) with 1% 3-aminopropyl triethoxy-silane (Sigma-Aldrich) ethanol solution. The colloid solutions were first diluted with 18.2-M Ω pure water to proper concentrations. Then the diluted solution was sonicated for 15 min at room temperature. After sonication, 6 μ L of the gold nanoparticle solution was added onto the modified coverslip, and the particles (citrate-capped, negatively charged) adsorb to the coverslip surface through electrostatic interactions.

Imaging System. An upright Nikon Eclipse 80i microscope was used in our investigations. The DIC mode used a pair of Nomarski prisms, a 100 \times Plan Apo/1.40 oil-immersion objective, and an NA 1.40 oil condenser, while the dark-field mode used a 100 \times Plan Fluor NA 0.7–1.3 oil objective and an NA 1.20–1.43 oil dark-field condenser. A high transmission 540-nm optical filter (Semrock, Rochester, NY) with a bandwidth of 20 nm was inserted at the illumination side. Before imaging, in order to differentiate gold nanoparticles from subcellular organelles, a high transmission 720-nm optical filter (Semrock, Rochester, NY) with a bandwidth of 13 nm was used because gold nanospheres that were visible at 540 nm would become nearly invisible at 720 nm as we have demonstrated previously.⁴⁴ The images and movies were taken by either a CoolSnap ES CCD camera (Photometrics, CA) or a Hamamatsu ORCA-Flash2.8 CMOS camera. An optimal combination of image contrast, spatial resolution, and temporal resolution was achieved with the imaging rate of 10 frames per second, which was used in all of our imaging experiments unless noted.

3D Imaging. A motorized rotary stage from Sigma Koki (model no. SGSP-60YAM) was coupled to the fine-adjustment knob on the microscope. The motor was controlled by Intelligent Driver, CSG-602R (Sigma Koki). The camera and stage were synchronized by adjusting the scanning speed and imaging rate. At the imaging rate of 10 frames per second, the distance between two successive images was 40 nm. MATLAB and NIH ImageJ were used to analyze and process the collected images and videos. The 3D images were rendered in Visage Imaging Amira (Berlin, Germany).

Surface Modification of Gold Nanoparticles. To facilitate their internalization into A549 cells, the gold nanoparticles were modified with either transferrin⁴⁵ or a cell penetrating peptide (CPP) from the HIV-1 protein Tat^{30,46,47} (sequence: YGRKKRRQRRR, AnaSpec, San Jose, CA). A NHS-PEG disulfide linker (Sigma-Aldrich) was used by following a published protocol.⁴⁸ The NHS-PEG disulfide linker has both disulfide and succinimidyl functionalities for respective chemisorption onto gold and facile covalent coupling of transferrin molecules. Briefly, a proper amount of fresh NHS-PEG disulfide solution (in dimethyl sulfoxide) was added to reach a final thiol concentration of 0.2 mM and reacted with gold nanoparticles for 2 h. The solution was then cleaned up by centrifugation and resuspended in 2 mM borate buffer. 2.0 μ g of transferrin (or 2.0 μ g of Tat CPP) was added to the gold

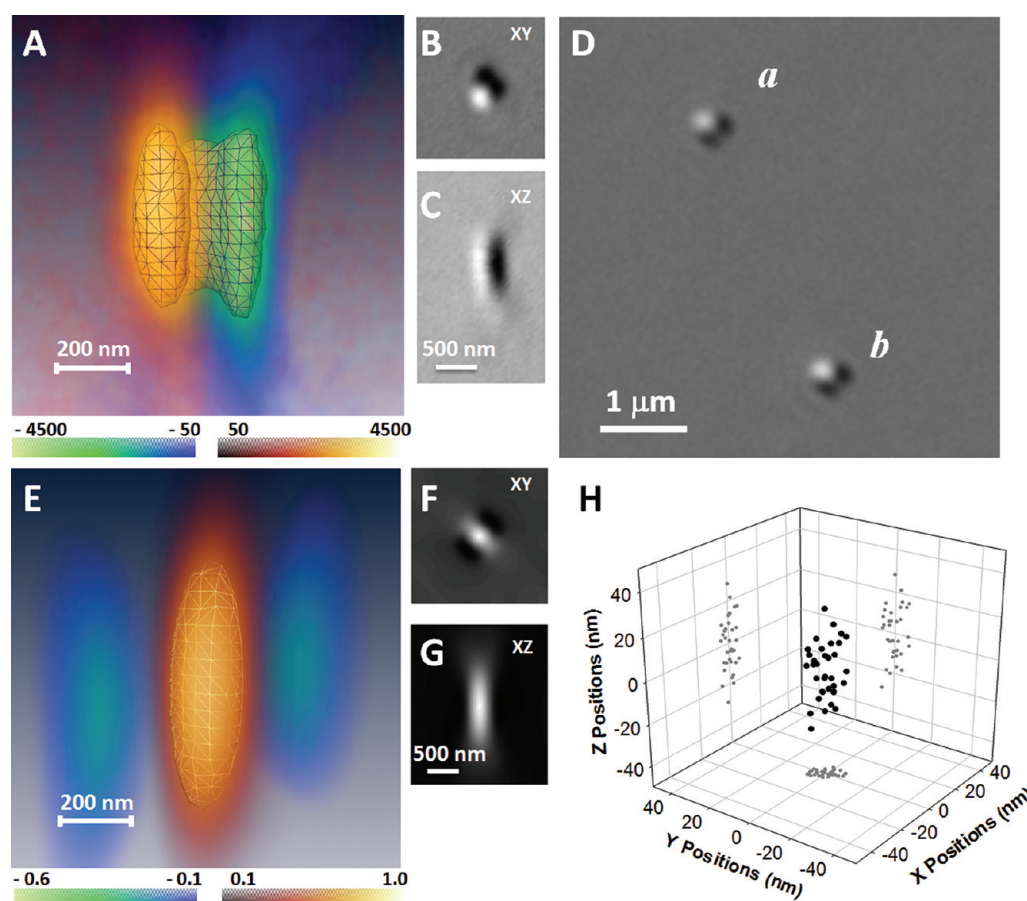


Figure 1. Model-based 3D correlation imaging for 3D super localization of gold nanoparticles. (A) 3D intensity profile of a 40-nm spherical gold nanoparticle immobilized on glass surface (shown in (D)) imaged with a 100 \times objective. The model is comprised of a bright portion shown in orange and a dark portion shown in blue. The 3D intensity profile was built from 65 equally spaced 2D DIC images along the optical axis. The pixel size was 36.3 nm, and the z-step was 40 nm. Ortho-slices of the image volume were shown in (B) and (C). (E) Model-based 3D correlation map of a 40-nm gold nanoparticle and its surrounding area. Ortho-slices of the correlation map were shown in (F) and (G). (H) Variations on the measured distance between two 40-nm gold particles from 42 sets of z-scans. The distance, rather than the absolute positions, was determined in order to eliminate the sample drifting in high precision microscopy. A correlation coefficient threshold of 0.6 (the shaded iso-surface in (E)) was used in the calculation.

colloidal solution and reacted for 8 h. Before use, the colloidal gold nanoparticles were cleaned up by centrifugation and resuspended in 2 mM borate buffer. The concentrated gold colloidal solution was diluted to a final concentration of 4.3×10^9 particles/mL for incubation with cells.

Cell Cultures and Imaging. For the localization of gold nanoparticles inside fixed cells, HeLa cells (ATCC, Manassas, VA) were cultured on 22 mm \times 22 mm poly-L-lysine coated glass coverslips in Petri dishes. 1.5 mL of minimum essential cell culture medium (ATCC) with 10% fetal bovine serum supplement was added to the plates. The cell culture was incubated at 37 $^{\circ}$ C under 5% CO₂. After the cell culture covered 70% of a coverslip, 30 μ L of TAT CPP-modified gold nanoparticle solution was added into the Petri dish and incubated with the cells for an hour. The gold nanoparticles were naturally internalized by the HeLa cells. The coverslip was then rinsed with 10 mM phosphate buffered saline (PBS) at pH 7.4, and then the cells were fixed with 4% paraformaldehyde in the same PBS buffer. After that, the cell coverslip was placed on a clean glass slide for observation. Two pieces of double-sided tape served as spacers between the glass slide and coverslip to form a chamber.

For the localization of gold nanoparticles during the endocytosis process, A549 human lung cancer cells (ATCC, CCL-185) were cultured on 22 mm \times 22 mm poly-L-lysine coated glass coverslips in Petri dishes. Minimum essential cell culture medium (ATCC) with 10% fetal bovine serum supplement was added to the plates. The cell culture was incubated at 37 $^{\circ}$ C under 5% CO₂. After the cell culture covered 70% of a coverslip, the cell coverslip was taken out for imaging, and a chamber was made using two pieces of double-sided tape. Twenty μ L of transferrin-modified gold nanoparticle solution was added into the chamber. The back-and-forth vertical scans and movie recording started immediately.

RESULTS AND DISCUSSION

Complexity of 3D DIC Point Spread Function. The 2D amplitude PSF of a DIC microscope adopts the form of^{44,49}

$$h(x, y) = (1 - R)e^{-i\theta}k(x - \Delta x, y) - Re^{i\theta}k(x + \Delta x, y) \quad (3)$$

where (x, y) is a point in the image plane, R is the amplitude ratio of the 2 illumination beams, $k(x, y)$ is the amplitude PSF for transmission optics under coherent illumination, 2θ is the additional phase bias, and the shear distance $2\Delta x$ is assumed to

be along the x direction without losing generality. In the image plane, the intensity distribution of a DIC image is the square modulus of the convolution of the DIC PSF and the object amplitude and phase distribution.

The 3D DIC PSF has been modeled by Preza and co-worker using eq 3 and the defocused PSF for transmission optics.^{49,50} Their work shows that under ideal conditions, i.e., the two illumination beams are of equal intensity and the phase bias 2θ is $\pi/2$, the 3D PSF is antisymmetric, i.e., it has a 2-fold rotation-reflection axis. However, due to nonideal experimental parameters, the actual 3D DIC PSF is more complicated. To demonstrate this, we collected the 3D intensity profile of a 40-nm gold nanosphere immobilized on a piece of glass coverslip with a z -step size of 40 nm. Figure 1A shows the 3D intensity profile, where the “hot” part shows the bright DIC intensities and the “cold” part shows the dark DIC intensities. Interestingly, the 3D PSF is elongated due to the lower resolution in the z -direction than in the x -, y -directions. Figure 1B and C shows the ortho-slices of the 3D intensity profile in the x - y and x - z planes, respectively. The dark part of the DIC image shows two minima in the focal plane and apparently not following the ideal antisymmetric pattern. In addition, the 3D DIC intensity profile is not symmetric along the z -direction with respect to the focal plane, and the bright and dark portions have different maximum/minimum at different z -positions.

Model-Based Correlation Imaging. To precisely locate 40-nm gold nanoparticle probes in biological samples, an experimental 3D DIC intensity profile of a nanoprobe is used as the model to map the nanoparticle probes in a stack of z -sectioned sample images. In practice, the sample containing the model nanoparticle and other nanoparticle probes are scanned vertically until a z -stack of images of a volume of interest is collected. The 3D model is cropped and then overlaid with a portion of the volume of interest. A correlation score is calculated to evaluate how likely the overlaid volume contains a nanoprobe. The model is then moved pixel by pixel, line by line, and frame by frame to cover the whole volume of interest. The correlation scores are calculated at each position and used to construct a 3D correlation map. The correlation scores can be defined through a variety of ways⁵¹ and herein Pearson's correlation coefficient was used. The correlation coefficient p between a 3D model and the subvolume that the model overlays is defined as

$$p(\text{model, sub-volume}) = \frac{1}{m-1} \sum_{i=1}^m \frac{[I_{\text{model}}(i) - I_{\text{model}}(\text{avg})]}{\sigma_{\text{model}}} \frac{[I_{\text{sub-volume}}(i) - I_{\text{sub-volume}}(\text{avg})]}{\sigma_{\text{sub-volume}}} \quad (4)$$

where the summation is over all the pixels in the 3D model or the subvolume, and m is the total number of pixels in the model; I is intensity; avg and σ denote the average and standard deviation of all intensities in the model or the subvolume, respectively. From the 3D correlation map, the position of a nanoparticle can be precisely located. The center of a nanoparticle can be computed by weighing all the coordinates that the particle covers with their corresponding p values

$$X_{\text{center}} = \frac{\sum_{i=1}^m X_i [p(i) - \text{Threshold}]}{\sum_{i=1}^m [p(i) - \text{Threshold}]} \quad (5)$$

where X can denote any Cartesian coordinates, x , y , or z , and a threshold is usually applied to cut off the noise contribution. The summation is over all the pixels that a particle covers. Through this weighing procedure, all intensities in the 3D profile are considered, and a subpixel precision can be obtained.

Figure 1D-H shows the localization of a 40-nm gold nanosphere using this model-based correlation imaging technique. In the localization, one stationary particle is selected as the reference in order to eliminate the error caused by the drifting of the sample relative to the microscope optics. That is, the position of the target particle relative to the reference particle is recorded. Figure 1E shows the 3D correlation map of the 40-nm gold nanoparticle and its surrounding area. High correlation scores close to its center are clearly identifiable (hot part). Similar to the 3D PSF, the 3D correlation coefficient map is also elongated along the z -direction. By setting a proper display threshold, the correlation scores appear as a spheroid shaped volume. Figure 1F and G shows the ortho-slices of the 3D map in the x - y and x - z planes, respectively. It is interesting to note that the central high correlation portion is flanked by two regions with low correlation scores (cold parts). The negative correlation scores mean anticorrelation, which is originated from the overlap of the bright part of the model and the dark part of the sample, or vice versa.

The centroid of the particle is determined by weighing the coordinates with the correlation scores using eq 5. In practice, a threshold is set to remove the interference from noise. Since the position is acquired from the whole image volume, high lateral and axial precisions are achieved. Figure 1H shows 42 repeated measurements of the position of particle a with respect to particle b . The standard deviations of the relative x , y , and z positions of particle a are 4.4, 6.5, and 16.0 nm, respectively. The axial localization precision is ~ 3 times of that in the x or y direction, consistent with the fluorescence-based methods.

The signal-to-noise ratio of DIC images plays an important role in localization precision. In the current study, DIC images of fixed 40-nm gold nanospheres were captured at 10 frames per second, which gave a signal-to-noise ratio of ~ 20 . Here the signal is defined as the intensity difference between the bright part and dark part for an in-focus 40-nm gold nanoparticle, and the noise is simply the standard deviation of the nonsignal background. Correspondingly, the temporal resolution of 3D superlocalization was in the range of seconds for taking stacks of z -slices at 40-nm steps through the sample volume. It is expected that the precision can be improved if the temporal resolution requirement is relaxed. For example, when the frame rate was halved to 5 frames per second, the x , y , and z localization precisions were improved to 3.1, 3.8, and 12.9 nm, respectively.

It is worthwhile to note that the mapping algorithm requires that the gold nanospheres are uniform in shape and size; otherwise, the 3D model generated from one particle may not fit accurately with the 3D images of other particles. The 40-nm gold nanoparticles used in the present study were sufficiently uniform to meet this requirement.

3D Localization of Gold Nanoparticles in Fixed Cells.

Gold nanoparticles have been reported to serve as carriers in targeted drug delivery,^{52,53} gene regulation⁵⁴ and photothermal therapies.⁵⁵ It is important to follow their distribution, trajectory, and final fate after they enter the host cell. To demonstrate the capability of the 3D correlation imaging, we further applied this 3D correlation mapping method in locating

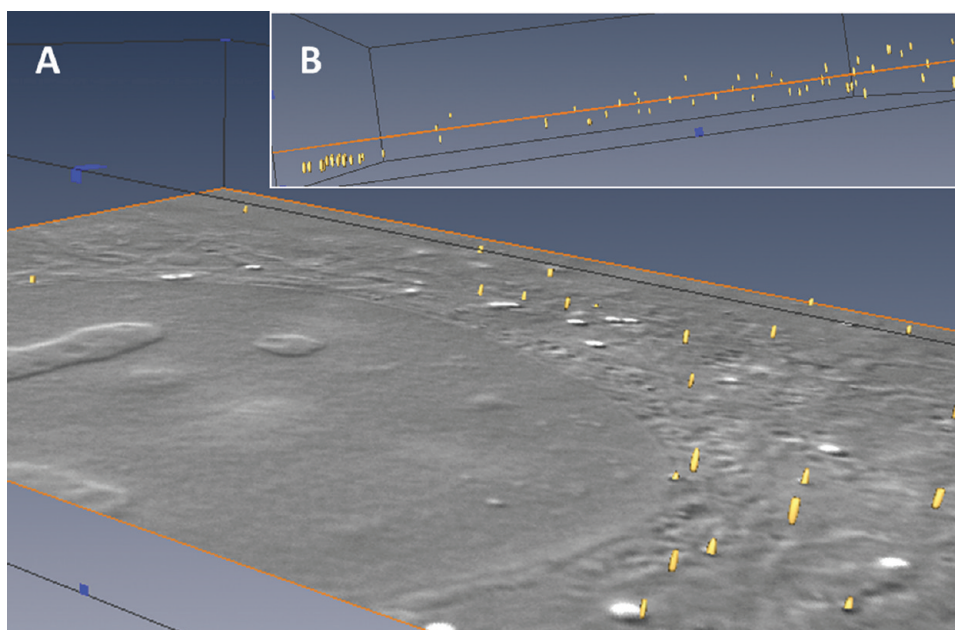


Figure 2. 3D localization of 40-nm gold nanoparticles inside a fixed HeLa cell. (A) The positions of mapped particles are presented as spheroid iso-correlation surfaces of 0.6 in the 3D correlation map. The cross section shows the DIC cell image at the corresponding position. (B) The same volume is viewed from a different angle to show that mapped particles are vertically distributed inside the cell. More slices of the cell image with vertically distributed gold nanoparticles are shown in Supplementary Figure 2.

and tracking 40-nm gold nanospheres in cells. We first demonstrated superlocalization of 40-nm gold nanoparticles in fixed HeLa cells.

The cells were incubated with Tat CPP-modified 40-nm gold nanoparticles for an hour to allow natural internalization to occur. The cells were then fixed using 4% glutaraldehyde for 20 min. Z-sections of the HeLa cells with gold nanoparticles were recorded (Supplementary Movie 1). Figure 2A shows the 3D distribution of mapped particles in a thin layer from the glass slide surface to $\sim 2\ \mu\text{m}$ above and their corresponding positions to a z-sectioned DIC image. It should be noted that the viewing angle is from above, and gold nanoparticles below the cell image are covered up and invisible. Gold nanospheres are displayed as elongated, golden iso-surfaces in the figure. All of the visible gold nanoparticles are in cell plasma and outside of the nucleus, with a few residing at locations very close to the nucleus membrane. This is consistent with the literature reports that gold nanoparticles larger than 20 nm will not go through the nucleus membrane.³⁰ Figure 2B shows the same cell viewed from the side. In the lower left corner, there are a group of gold nanoparticles in the same plane. Those are adsorbed particles on the glass coverslip.

One thing to note is that the automated localization procedure can also pick up other spherical subcellular organelles that have a 3D DIC intensity profile similar to that of the gold nanoparticle model. In order to discriminate single gold nanoparticle probes from these spherical structures, as well as nanoparticle aggregates, with high confidence, we also imaged the cell at 720 nm at which single gold nanoparticles could be “switched off” to manually exclude those cellular structures and larger aggregates.³¹

3D Localization of Gold Nanoparticles in Live Cells.

The applicability of the 3D correlation mapping algorithm to single particle tracking in live cells was further demonstrated by tracking 40-nm transferrin-modified gold nanoparticles continuously during their internalization by live A549 cells.

Transferrin and transferrin-modified gold nanospheres are known to be internalized by cells mainly through clathrin-mediated endocytosis.^{57,58} When incubated with cells, the negatively charged nanoparticles can be adsorbed on the cell membrane through nonspecific adsorption and/or specific receptor binding and perform active translational diffusion on the cell membrane. The particles then either dissociate from the cell surface or are temporarily fixed at one location presumably by specific interactions with transferrin receptors before the internalization occurs. The endocytosis process usually takes several minutes, after which the nanoparticles restore active translational motion, including intracellular transport and random diffusion, inside the cell.

In our tracking experiment, some of the negatively charged gold nanoparticles were firmly adsorbed on the positively charged poly-L-lysine-modified coverslip surface through electrostatic attraction. One such particle was chosen as the reference (Figure 3A) to eliminate the effect of sample drifting during the repeated vertical scans. The relative 3D position of the particles of interest (Figure 3B) was tracked continuously by repeatedly scanning between the coverslip surface and the top cell surface.

The tracking started when the particle stopped active translational diffusion on cell membrane and stayed at a relatively fixed position, allowing its location to be measured with sufficient accuracy. The 3D moving trace of the gold nanoparticle (Figure 3C) shows clearly that the particle moved significantly before it finally entered the cells. The movement in the z-direction was as large as several hundred nanometers between data points, much larger than the cell membrane thickness (5–10 nm). The big position changes in the z-direction are possibly due to the movement of the cell membrane or the change of the cell surface morphology. At the end of the endocytosis, the nanoparticle went into the cells and diffused away from the original entry spot.

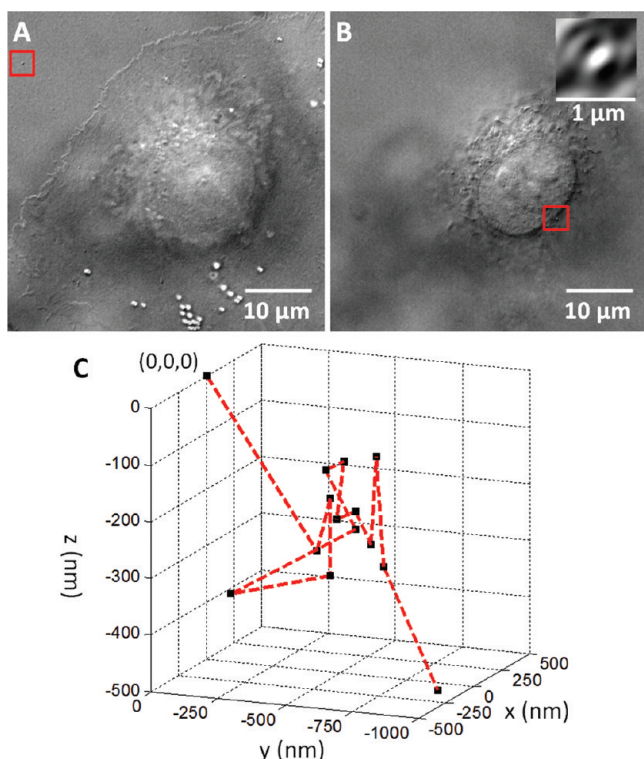


Figure 3. The 3D trajectory of a gold nanoparticle on the membrane of an A549 cell. (A) The reference particle adsorbed on the coverslip. (B) The particle of interest on the cell membrane. The correlation map for this particle (the imbedded image) consists of a bright center and two dark side lobes, similar to the one shown in Figure 1F. These particles are imaged in different focal planes. (C) The moving trace of the nanoparticle. The initial position of the particle was (0, 0, 0). Larger z coordinates indicate the particle was closer to the cell surface and farther away from the coverslip.

Achievable Temporal Resolution. Temporal resolution is an important consideration in tracking dynamic biological events. The temporal resolution for a recorded sequence of nanoparticle movement is simply the time spent on one vertical scan through the sample of interest. In the endocytosis study, the whole depth of the cell ($\sim 6.4 \mu\text{m}$) was scanned with a step size of 40 nm and an image exposure time of 100 ms. This yields a temporal resolution of 16 s for each particle position in order to achieve a sub-20 nm spatial resolution. This temporal resolution may not be sufficient for fast dynamics, such as the Brownian motion or intracellular transport on the cytoskeleton tracks. However, it is generally adequate for localizing nanoparticles with restricted movement when they are imbedded in viscous media such as cell membranes or bound to relatively stationary organelles. Because this method has minimal intrusion to biological systems and no photobleaching, it is ideal for long-term high-precision tracking of nanoprobe in living systems.

The temporal resolution of this method can be improved to ~ 1 s without sacrificing localization precision. Note that a large fraction of time was spent in scanning through the nonsignal regions (area contains no probe or target of interest). If we reduce the scanning depth to ~ 400 nm, which is sufficient to cover the image volume of a visible nanoparticle, we can achieve a temporal resolution of 1 data point per second under the same experimental conditions (100 ms exposure time and 40 nm vertical step size). This temporal resolution is

comparable to most commercially available confocal fluorescence microscopes with a temporal resolution on the order of 1 frame per second for collecting 2D images.

Limitations of the Technique. Just like other localization techniques, the model-based 3D mapping technique also has its limitations. First, this technique requires that the nanoparticles are well separated, i.e., their distance is larger than the diffraction limit. This is rather an intrinsic limitation for all far-field light microscopy techniques. Second, this technique requires a high consistency in the morphology of nanoparticles because of the imaging principles of DIC microscopy. This is the challenge and also the opportunity for the development of current nanotechnology.

CONCLUSIONS

In summary, a 3D model-based correlation mapping method was developed to locate gold nanoparticles through vertical scans of the sample volume of interest. This localization method provides sub-20-nm axial precision. Using this method, 40-nm gold nanoparticles in a fixed HeLa cell were detected, and their positions were mapped in the 3D cellular environment. Dynamic tracking of gold nanoparticles on the live cell membrane during the endocytosis process was also demonstrated. Although with limitations, this 3D localization method allows long-term single particle tracking with high precision and thus has a high potential in studying biological processes where precise localization is essential in learning the mechanisms.

ASSOCIATED CONTENT

Supporting Information

Additional information as noted in text. This material is available free of charge via the Internet at <http://pubs.acs.org>.

AUTHOR INFORMATION

Corresponding Author

*G.W.: Fax: (+1) 919-515-8909. E-mail: gufeng_wang@ncsu.edu. N.F.: Fax: (+1) 515-294-0105. E-mail: nfang@iastate.edu.

Notes

The authors declare no competing financial interest.

ACKNOWLEDGMENTS

This work was supported by the U.S. Department of Energy, Office of Basic Energy Sciences, Division of Chemical Sciences, Geosciences, and Biosciences through the Ames Laboratory and in part by the North Carolina State University start-up funds to G.W. The Ames Laboratory is operated for the U.S. Department of Energy by Iowa State University under contract no. DE-AC02-07CH11358.

REFERENCES

- (1) Waga, S.; Stillman, B. *Annu. Rev. Biochem.* **1998**, *67*, 721.
- (2) Kural, C.; Kim, H.; Syed, S.; Goshima, G.; Gelfand, V. I.; Selvin, P. R. *Science* **2005**, *308*, 1469.
- (3) Forkey, J. N.; Quinlan, M. E.; Shaw, M. A.; Corrie, J. E. T.; Goldman, Y. E. *Nature* **2003**, *422*, 399.
- (4) Yasuda, R.; Noji, H.; Yoshida, M.; Kinosita, K.; Itoh, H. *Nature* **2001**, *410*, 898.
- (5) Nan, X. L.; Sims, P. A.; Chen, P.; Xie, X. S. *J. Phys. Chem. B* **2005**, *109*, 24220.
- (6) Murase, K.; Fujiwara, T.; Umemura, Y.; Suzuki, K.; Ino, R.; Yamashita, H.; Saito, M.; Murakoshi, H.; Ritchie, K.; Kusumi, A. *Biophys. J.* **2004**, *86*, 4075.

- (7) Thompson, R. E.; Larson, D. R.; Webb, W. W. *Biophys. J.* **2002**, 82, 2775.
- (8) Toprak, E.; Balci, H.; Blehm, B. H.; Selvin, P. R. *Nano Lett.* **2007**, 7, 2043.
- (9) Huang, B.; Wang, W. Q.; Bates, M.; Zhuang, X. W. *Science* **2008**, 319, 810.
- (10) Juette, M. F.; Gould, T. J.; Lessard, M. D.; Mlodzianoski, M. J.; Nagpure, B. S.; Bennett, B. T.; Hess, S. T.; Bewersdorf, J. *Nat. Methods* **2008**, 5, 527.
- (11) Shtengel, G.; Galbraith, J. A.; Galbraith, C. G.; Lippincott-Schwartz, J.; Gillette, J. M.; Manley, S.; Sougrat, R.; Waterman, C. M.; Kanchanawong, P.; Davidson, M. W.; Fetter, R. D.; Hess, H. F. *Proc. Natl. Acad. Sci. U. S. A.* **2009**, 106, 3125.
- (12) Bates, M.; Huang, B.; Dempsey, G. T.; Zhuang, X. W. *Science* **2007**, 317, 1749.
- (13) Betzig, E.; Patterson, G. H.; Sougrat, R.; Lindwasser, O. W.; Olenych, S.; Bonifacio, J. S.; Davidson, M. W.; Lippincott-Schwartz, J.; Hess, H. F. *Science* **2006**, 313, 1642.
- (14) Westphal, V.; Rizzoli, S. O.; Lauterbach, M. A.; Kamin, D.; Jahn, R.; Hell, S. W. *Science* **2008**, 320, 246.
- (15) Xie, X. S.; Dunn, R. C. *Science* **1994**, 265, 361.
- (16) Moerner, W. E.; Orrit, M. *Science* **1999**, 283, 1670.
- (17) Nirmal, M.; Dabbousi, B. O.; Bawendi, M. G.; Macklin, J. J.; Trautman, J. K.; Harris, T. D.; Brus, L. E. *Nature* **1996**, 383, 802.
- (18) Derfus, A. M.; Chan, W. C. W.; Bhatia, S. N. *Nano Lett.* **2004**, 4, 11.
- (19) Wang, G. F.; Stender, A. S.; Sun, W.; Fang, N. *Analyst* **2010**, 135, 215.
- (20) West, J. L.; Halas, N. J. *Annu. Rev. Biomed. Eng.* **2003**, 5, 285.
- (21) Murphy, C. J.; Gole, A. M.; Stone, J. W.; Sisco, P. N.; Alkilany, A. M.; Goldsmith, E. C.; Baxter, S. C. *Acc. Chem. Res.* **2008**, 41, 1721.
- (22) De, M.; Ghosh, P. S.; Rotello, V. M. *Adv. Mater.* **2008**, 20, 4225.
- (23) Saxton, M. J.; Jacobson, K. *Annu. Rev. Biophys. Biomol. Struct.* **1997**, 26, 373.
- (24) Debrabander, M.; Nuydens, R.; Geuens, G.; Moeremans, M.; Demey, J. *Cell Motil. Cytoskeleton* **1986**, 6, 105.
- (25) Hu, M.; Novo, C.; Funston, A.; Wang, H. N.; Staleva, H.; Zou, S. L.; Mulvaney, P.; Xia, Y. N.; Hartland, G. V. *J. Mater. Chem.* **2008**, 18, 1949.
- (26) Rong, G. X.; Wang, H. Y.; Skewis, L. R.; Reinhard, B. M. *Nano Lett.* **2008**, 8, 3386.
- (27) Boyer, D.; Tamarat, P.; Maali, A.; Lounis, B.; Orrit, M. *Science* **2002**, 297, 1160.
- (28) Cognet, L.; Tardin, C.; Boyer, D.; Choquet, D.; Tamarat, P.; Lounis, B. *Proc. Natl. Acad. Sci. U. S. A.* **2003**, 100, 11350.
- (29) Lasne, D.; Blab, G. A.; Berciaud, S.; Heine, M.; Groc, L.; Choquet, D.; Cognet, L.; Lounis, B. *Biophys. J.* **2006**, 91, 4598.
- (30) Tkachenko, A. G.; Xie, H.; Liu, Y. L.; Coleman, D.; Ryan, J.; Glomm, W. R.; Shipton, M. K.; Franzen, S.; Feldheim, D. L. *Bioconjugate Chem.* **2004**, 15, 482.
- (31) Sun, W.; Wang, G.; Fang, N.; Yeung, E. S. *Anal. Chem.* **2009**, 81, 9203.
- (32) Shah, N. B.; Dong, J.; Bischof, J. C. *Mol. Pharmaceutics* **2010**, 8, 176.
- (33) Ando, J.; Fujita, K.; Smith, N. I.; Kawata, S. *Nano Lett.* **2011**, 11, 5344.
- (34) Wang, G. F.; Sun, W.; Luo, Y.; Fang, N. *J. Am. Chem. Soc.* **2010**, 132, 16417.
- (35) Gu, Y.; Sun, W.; Wang, G. F.; Fang, N. *J. Am. Chem. Soc.* **2011**, 133, 5720.
- (36) Sun, W.; Fang, N.; Trewyn, B. G.; Tsunoda, M.; Slowing, I. I.; Lin, V. S. Y.; Yeung, E. S. *Anal. Bioanal. Chem.* **2008**, 391, 2119.
- (37) Sherry, L. J.; Chang, S. H.; Schatz, G. C.; Van Duyne, R. P.; Wiley, B. J.; Xia, Y. N. *Nano Lett.* **2005**, 5, 2034.
- (38) Lee, K. J.; Nallathamby, P. D.; Browning, L. M.; Osgood, C. J.; Xu, X.-H. N. *ACS Nano* **2007**, 1, 133.
- (39) Tsunoda, M.; Isailovic, D.; Yeung, E. S. *J. Microsc. (Oxford, U. K.)* **2008**, 232, 207.
- (40) Li, H. W.; McCloskey, M.; He, Y.; Yeung, E. S. *Anal. Bioanal. Chem.* **2007**, 387, 63.
- (41) Tsunoda, M.; Isailovic, D.; Yeung, E. S. *J. Microsc. (Oxford, U. K.)* **2008**, 232, 207.
- (42) Pluta, M. *Advance light microscopy*; Elsevier Science Publishing Co. Inc.: New York, 1989; Vol. 2.
- (43) Gelles, J.; Schnapp, B. J.; Sheetz, M. P. *Nature* **1988**, 331, 450.
- (44) Sun, W.; Wang, G. F.; Fang, N.; Yeung, E. S. *Anal. Chem.* **2009**, 81, 9203.
- (45) Qian, Z. M.; Li, H. Y.; Sun, H. Z.; Ho, K. *Pharmacol. Rev.* **2002**, 54, 561.
- (46) de la Fuente, J. M.; Berry, C. C. *Bioconjugate Chem* **2005**, 16, 1176.
- (47) Heitz, F.; Morris, M. C.; Divita, G. *Br. J. Pharmacol.* **2009**, 157, 195.
- (48) Narayanan, R.; Lipert, R. J.; Porter, M. D. *Anal. Chem.* **2008**, 80, 2265.
- (49) Preza, C.; Snyder, D. L.; Conchello, J. A. *J. Opt. Soc. Am. A* **1999**, 16, 2185.
- (50) Gibson, S. F.; Lanni, F. *J. Opt. Soc. Am. A* **1989**, 6, 1357.
- (51) Wang, G. F.; Geng, L. *Anal. Chem.* **2005**, 77, 20.
- (52) Qian, X. M.; Peng, X. H.; Ansari, D. O.; Yin-Goen, Q.; Chen, G. Z.; Shin, D. M.; Yang, L.; Young, A. N.; Wang, M. D.; Nie, S. M. *Nat. Biotechnol.* **2008**, 26, 83.
- (53) Liong, M.; Lu, J.; Kovichich, M.; Xia, T.; Ruehm, S. G.; Nel, A. E.; Tamanoi, F.; Zink, J. I. *ACS Nano* **2008**, 2, 889.
- (54) Rosi, N. L.; Giljohann, D. A.; Thaxton, C. S.; Lytton-Jean, A. K. R.; Han, M. S.; Mirkin, C. A. *Science* **2006**, 312, 1027.
- (55) Lal, S.; Clare, S. E.; Halas, N. J. *Acc. Chem. Res.* **2008**, 41, 1842.
- (56) De Jong, W. H.; Hagens, W. I.; Krystek, P.; Burger, M. C.; Sips, A.; Geertsma, R. E. *Biomaterials* **2008**, 29, 1912.
- (57) Klausner, R. D.; Vanrenswoude, J.; Ashwell, G.; Kempf, C.; Schechter, A. N.; Dean, A.; Bridges, K. R. *J. Biol. Chem.* **1983**, 258, 4715.
- (58) Chithrani, B. D.; Chan, W. C. W. *Nano Lett.* **2007**, 7, 1542.